Research Article Vol. 33, No. 10 / 19 May 2025 / Optics Express 21938

Optics EXPRESS

Subwavelength 3D terahertz imaging with a single-pixel laser transceiver

JORGE SILVA,[1] MARTIN PLÖSCHNER,[1] KARL BERTLING,[1] MUKUND GHANTALA,[1] TIM GILLESPIE,[1] JARI TORNIAINEN,[1] JEREMY HERBERT,[1] YAH LENG LIM,[1] THOMAS TAIMRE,[2] XIAOQIONG QI,[1] BOGDAN C. DONOSE,[1] TAO ZHOU,[1] HOI-SHUN LUI,[1] DRAGAN INDJIN,[3] YINGJUN HAN,[3] LIANHE LI,[3] ALEXANDER VALAVANIS,[3] EDMUND H. LINFIELD,[3] A. GILES DAVIES,[3] PAUL DEAN,[3] AND ALEKSANDAR D. RAKIĆ[1,*]

[1] *School of Electrical Engineering and Computer Science, The University of Queensland, Brisbane, 4072 Queensland, Australia*
[2] *School of Mathematics and Physics, The University of Queensland, Brisbane, 4072 Queensland, Australia*
[3] *School of Electronic and Electrical Engineering, University of Leeds, Leeds LS2 9JT, UK*
[*] *a.rakic@uq.edu.au*

Abstract: Terahertz imaging holds great potential for non-destructive material inspection, but practical implementation has been limited by resolution constraints. In this study, we present a single-pixel THz imaging system based on a confocal microscope architecture, utilizing a quantum cascade laser as both transmitter and phase-sensitive receiver. We demonstrate, for the first time to the best of our knowledge, that laser feedback interferometry-based imaging systems achieve enhanced lateral and axial resolution compared to conventional confocal imaging. Specifically, our approach yields a twofold improvement in lateral resolution, reaching $\lambda/2$, and a two-order-of-magnitude enhancement in axial resolution, from 25λ to beyond $\lambda/5$, through interferometric phase detection. The system can produce a 0.5 megapixel image in under three minutes, surpassing both raster-scanning single-pixel and multipixel focal-plane array-based imagers. Coherent operation enables simultaneous amplitude and phase image acquisition, and a custom visualization method links amplitude to image saturation and phase to hue, enhancing material characterization. A 3D tomographic analysis of a silicon chip reveals subwavelength features, demonstrating the system's potential for high-resolution THz imaging and material analysis. This work overcomes the resolution limits of conventional lens-based imaging systems, by enabling rapid, high-fidelity imaging of subwavelength features beyond the diffraction limit.

1. Introduction

Terahertz (THz) radiation's unique ability to penetrate optically opaque materials makes it a powerful tool for noninvasive imaging of concealed objects and subsurface defects [1–6]. Its non-ionizing nature, low phototoxicity, and capacity to identify biological molecules through their unique "fingerprints" at THz frequencies make it an emerging tool in biosensing and medical diagnostics [7–10]. Additionally, THz imaging has been applied to study carrier dynamics in silicon wafers, organic solar cells, and for conductivity mapping of novel materials like graphene [11–14]. This rapidly expanding application space of THz imaging creates a burgeoning need for more compact technology with higher spatial and temporal resolution, as well as enhanced material specificity. However, current THz technology struggles to meet all these demands simultaneously.

#561713 https://doi.org/10.1364/OE.561713
Journal © 2025 Received 10 Mar 2025; revised 24 Apr 2025; accepted 25 Apr 2025; published 15 May 2025

Optics EXPRESS

State-of-the-art THz multipixel cameras [15–17] capture only the intensity of THz radiation, neglecting the phase information essential to enhance imaging resolution and recover material properties like the complex refractive index. While digital holography [18–20] can be used in conjunction with THz cameras to retrieve the phase information, the process is slow, computationally challenging, and suffers from phase instabilities due to the need for a reference beam. Single-pixel detection schemes, especially those using time-domain spectroscopy (TDS) [21–23], overcome many of the limitations of multipixel cameras but still suffer from low spatial resolution and slow image formation.

Here, we demonstrate a single-pixel camera based on a terahertz confocal microscope capable of high-resolution, high-frame-rate far-field THz imaging with a unique capacity for depth sectioning and a depth resolution exceeding $\lambda/5$. The system achieves compactness and ease of alignment through its incredibly simple design: a single laser used for both illumination and detection via laser feedback interferometry (LFI) [24]. Terahertz radiation from a quantum cascade laser (QCL) [25–27] is focused onto the sample for raster scanning. The reflected signal then travels back through the optical system and is reinjected into the QCL, which simultaneously functions as the detector, confocal pinhole, and illumination source. Combining these functions into a single device not only enables a compact design but also significantly simplifies system alignment [28]. We provide, to the best of our knowledge, the first comprehensive guide on how to implement and optimize this technology [29–33] to achieve optimal imaging performance. Through simulation of the beam propagation, we find the most favorable detection plane to be the QCL's front facet.

We show for the first time that LFI technology provides enhanced lateral and axial resolution over conventional imaging configurations, down to the subwavelength level. Recent work in THz interferometric imaging [34–38] has demonstrated impressive resolution, but have been restricted to improving either the lateral or axial resolutions independently, not both. Far-field THz imaging using confocal scanning systems have shown three-dimensional resolution improvement [39–41]. Here, we show an improvement to subwavelength resolution, achieving lateral resolution of $\lambda/2$ and axial resolution of $\lambda/5$. The system's point spread function (PSF), measured using a knife-edge technique, shows a better than twofold improvement in lateral and axial resolution over conventional systems, effectively surpassing the diffraction limit. This more than twofold improvement is attributed to two main factors: spatial filtering from the QCL acting as a confocal pinhole—analogous to pinhole filtering techniques used in confocal microscopy [42]—and the nonlinear relationship between detection and the target, similar to nonlinear biological microscopy [43,44]. The depth of focus (DOF) is further enhanced from 2.6 mm (or 25λ) to beyond $\lambda/5$ through phase information. We combine the high-resolution capability with a fast beam steering configuration to deliver a 0.5 Megapixel image in less than three minutes. This compares favorably with other reported imagers of both the raster scanning (single pixel) and multipixel focal-plane array based solutions, alike. To accommodate a wide range of applications requiring different scan areas, we also investigate the system's performance with different focusing objective numerical apertures. Finally, we illustrate the system's DOF resolution by performing 3D tomographic imaging of hidden features of a packaged silicon chip.

2. Operating principle

Imaging is achieved by integrating a detection scheme within the THz source, with transmission optics capturing reflected light from the sample back to the sensor, analogous to a camera lens (Fig. 1(a)). The detection principle, based on laser feedback interferometry, measures the interference between the QCL intracavity electric field and the reinjected radiation reflected from the sample [45], as shown in Fig. 1(b). This self-mixing (SM) effect produces a time-oscillating SM wave in the laser terminal voltage, allowing for the acquisition of amplitude and phase information [24,46]. Coherent 3D imaging is achieved through fast beam steering (Fig. 1(c)).

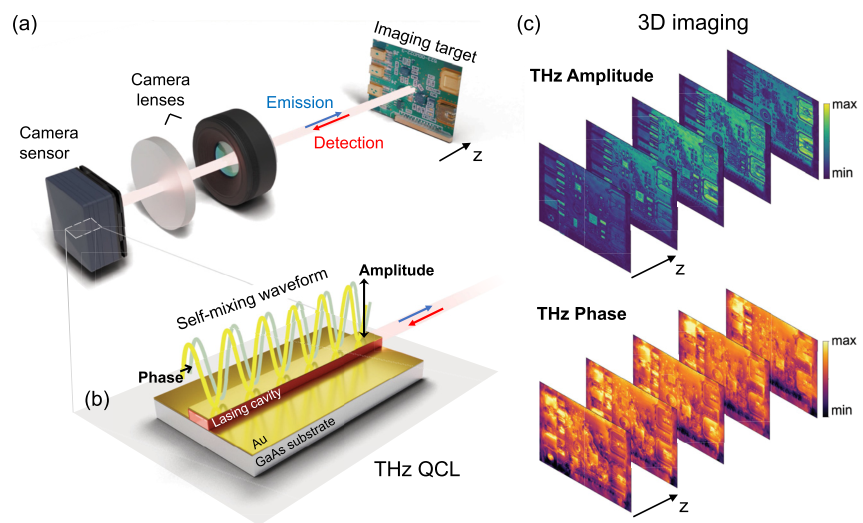

Fig. 1. (a) A camera-like imaging configuration is shown, where the laser source doubles as a sensor. The optical system collimates the laser beam and focuses it onto the sample. By adjusting the numerical aperture of the focusing lens, both the spot size and depth of focus are controlled. (b) The terahertz quantum cascade laser acts as the source for the self-mixing waveform. The self-mixing effect enables coherent imaging by providing both amplitude and phase information, forming the basis for high-resolution 3D imaging. (c) Fast beam steering enables rapid image acquisition and retrieval of 3D information [28]. This technique allows for the detailed inspection of internal structures, as demonstrated by 3D imaging of a packaged semiconductor chip.

3. System characterization and performance analysis

In essence, the confocal imaging setup consists of a THz QCL, a collimating lens (L1) of 30 mm focal length, and a focusing lens (L2) of 50 mm focal length (Fig. 2). The QCL is made of a periodic GaAs/AlGaAs quantum-well heterostructure, emitting at a frequency of 2.85 THz (λ = 105 μm) with a peak output power of 2 mW [47]. The emitted beam propagates through the optical system and is focused onto the imaging target, from which is then reflected, propagates back, and is reinjected into the laser cavity. Both measured and simulated field distributions at carefully selected planes L1, P1, P2, P3, and the imaging plane are shown in Fig. 2 and 3. The reinjection at the QCL is simulated in Fig. 4(a). Finally, the power loss along the optical system, in both the forward and return paths, is computed in Fig. 4(b). Experimental measurements were acquired with a pyroelectric detector, while simulations were coded in Python [48].

Simulated near-field and corresponding far-field distributions of the QCL are presented in Fig. 2(a). The optimal position of the collimating lens is found to be 27.8 mm from the QCL's front facet, as shown in Fig. 2(b). The appearance of concentric rings in Fig. 2(c) is due to a change in wavefront upon transmission through the L1 lens aperture (25 mm), as illustrated in Fig. 2(b). Figure 3 shows the 3D focused beam. Here, we explored the DOF and lateral beam extent through simulation and experiment (Fig. 3(a) for 2D and 3D field distributions near the focal point). Figure 3(b) displays the field distributions on both sides of the focal plane (the imaging plane). Beam characterization is conducted over a 2 mm axial range near the focal plane, where highly intense radiation (>50%) is confined. The beam shows a clean circular shape at focus, maintaining its form as it moves away from the focal plane, with some asymmetry due to the QCL's unfiltered emission profile. While further analysis, such as M^2 measurements, could

Optics EXPRESS

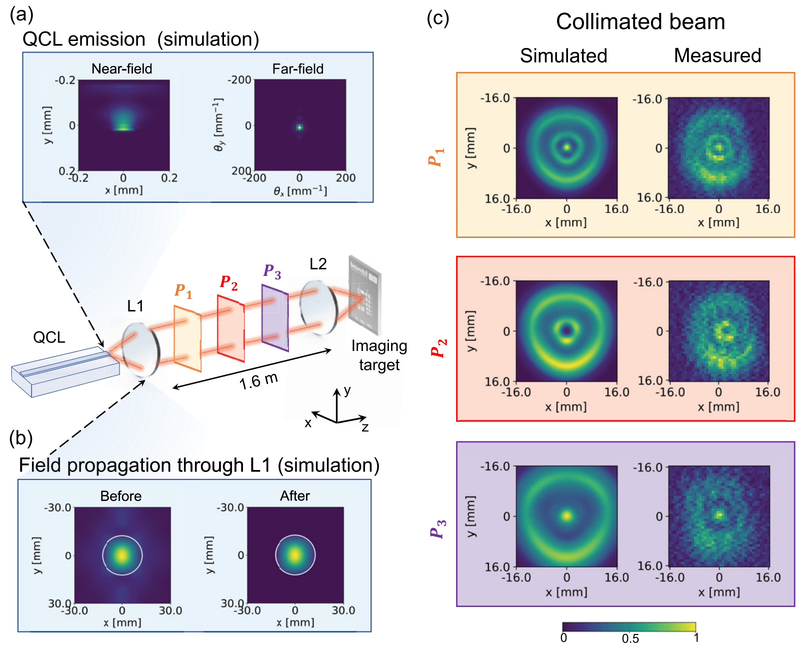

Fig. 2. QCL emission and collimation. (a) Simulated near-field and far-field QCL emission intensity profiles. The near-field profile corresponds to the QCL's front facet emission, for which we implement a FFT to compute the far-field. (b) Simulated field propagation through a 30 mm focal length lens L1 (Tsurupica-RR-CX-1.5-30-SPS, BBLaser Inc., Tokyo, Japan), where the white circle denotes the clear aperture of the lens (25 mm). (c) Simulated and measured collimated beam intensity profiles for three distinct planes located after the collimating lens L1, at a distance of 480 mm (P_1), 630 mm (P_2) and 930 mm (P_3) from the QCL's front facet.

be performed to assess beam quality, a qualitative analysis is sufficient for the purposes of this work, which prioritizes PSF measurements.

Finally, reinjection back into the QCL is mapped (Fig. 4(a)), showing optimal reinjection on the front facet of the QCL (z = 0 mm). The emission and reinjection profiles are compared, revealing that the reinjection extends beyond the waveguide region into the substrate. Power loss analysis (Fig. 4(b)) shows significant losses due to atmospheric absorption, Fresnel reflections, and beam clipping from apertures at L1 (25 mm) and L2 (30 mm). In backward propagation, atmospheric absorption, target reflectance, and reinjection at the QCL's front facet contribute more to power loss. Higher reinjected power does not always result in better image quality due to strong feedback that introduces noise and compromises the stability of the system [49,50]. To mitigate this, an attenuator (1/4 factor) was used to avoid beam pattern changes and reduce noise, improving system stability. This is an attractive feature towards imaging objects with low reflectivity or when working in an environment prone to scattering and absorption since it induces weak feedback regimes, translating to higher image quality and overall greater system stability. We would like to note that the reason for requiring a long optical path (≈ 1.6 m, Fig. 2) is that it gives us more SM fringes and therefore improved FFT frequency resolution [51]. However, a long optical path does not necessarily mean the system is large, as the optical path length can be reduced with folded mirror design - as implemented in our THz imaging system.

Optics EXPRESS

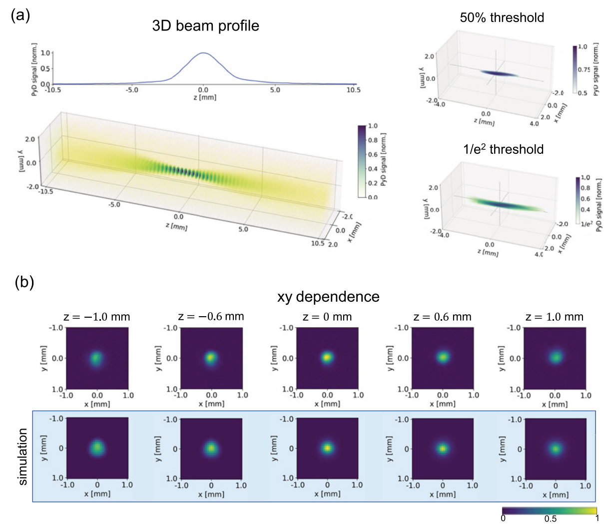

Fig. 3. Beam focusing onto the imaging plane. (a) Measured 3D profile of the beam focused by a 50 mm focal length lens L2 (Tsurupica-RR-CX-1.5-50-SPS, BBLaser Inc., Tokyo, Japan) onto the imaging plane (z = 0 mm). The regions of strongest signal (thresholds above 13.5% ($1/e^2$) and 50%) are subsequently mapped. (b) Measured and simulated xy beam profiles in the vicinity of the imaging plane.

4. Comparison between conventional and LFI imaging PSFs

The 3D PSF, representing the system's impulse response to a point light source, provides insights into the system's resolution properties [52] and is experimentally characterized for both conventional and LFI imaging (Fig. 5(a)). Using a knife-edge technique in transmission (PyD signal) and reflection (SM signal) configurations, we obtain the PSF in both imaging setups. Transmission represents conventional imaging, while reflection corresponds to LFI due to reinjected radiation into the laser cavity (see Section 5 of Supplement 1). Extending this procedure along the axial direction (z) allows the construction of 3D PSF measurements (Fig. 5(b)). Closer to the focusing lens, Gaussian profiles are observed, while multi-peak profiles emerge in the LFI PSF for positions farther away ($+z$ direction). The axial PSF and beam diameters are also measured (Fig. 5(c)). LFI systems show a narrower full width at half maximum (FWHM) by a factor of 1.5, improving axial resolution in 3D sectioning. Beam diameters in LFI-based systems are up to 2.3 times smaller, enhancing lateral resolution compared to conventional imaging. In regions of high overlap between focused and reinjected profiles (15% at z = 0.5 mm), lateral resolution improves by a factor of 1.6. Figure 5(d) illustrates this axial resolution improvement, with reinjected beam diameters (red line) overlaid on the xy focused beam profiles (Fig. 3(b)). Reinjection from high-intensity regions exhibits astigmatic behavior, leading to a mismatch between x and y beam diameters in axial propagation. To see how narrower PSFs translate to increased spatial resolution, in Section 5 we compute the system's maximum resolvable spatial frequency for different focusing optics.

5. Effect of numerical aperture on image resolution

The numerical aperture (NA) determines the acceptance angles for target illumination (Fig. 6(a)), significantly affecting both lateral and axial resolutions [53]. To assess this impact, 3D characterization of the focused beam is performed (Fig. 6(b)). Higher NA leads to increased divergence and a shorter Rayleigh length (θ = 19°, z_R = 2.3 mm for NA = 0.3; and θ = 30°,

Optics EXPRESS

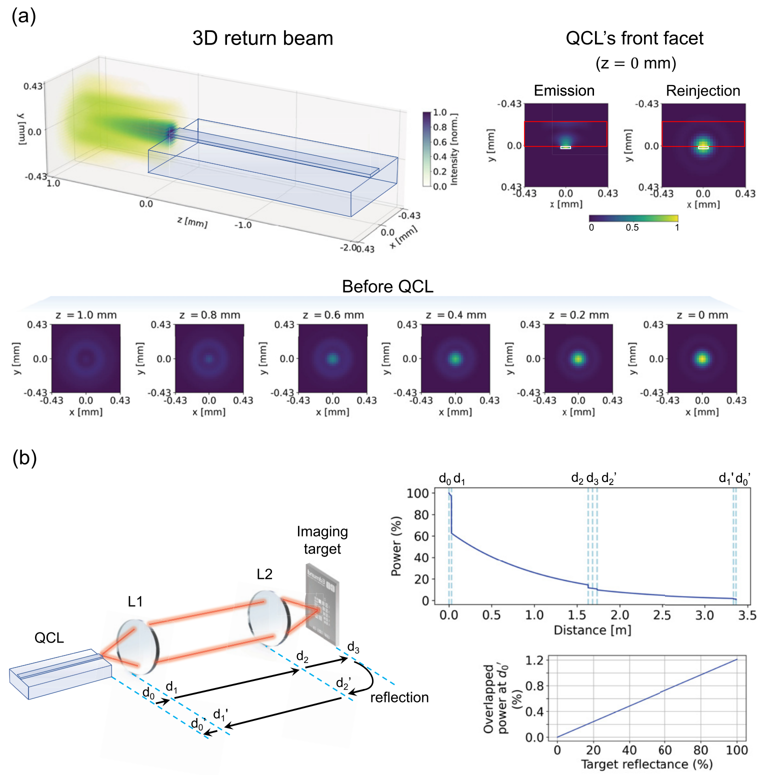

Fig. 4. Reinjection at the QCL and power loss along the optical system. (a) Simulated 3D reinjection profile at the QCL from the reflection of a mirror placed at the focal imaging plane (z = 0 mm in Fig. 3). Emission and reinjection profiles at the QCL's front facet (z = 0 mm) are displayed, with the white rectangle denoting the QCL's waveguide region and the red rectangle being the QCL's substrate. Several xy beam profiles are shown at different positions along the optical axis (z>0 mm). (b) Simulated power loss along the optical system. Power percentage relative to distance from the QCL's front facet is plotted by integrating 2D beam profiles. At d_0', the power is given by the overlap between emission and reinjection profiles. The change of reinjected power on the imaging target's reflectance is also computed.

z_R = 1.3 mm for NA = 0.5, Fig. 6(c)), improving lateral and axial resolutions. Higher NA improves axial resolution, with a factor of 1.7 improvement in LFI configurations ($FWHM_{PyD}$ = 4.3 mm = 41λ, $FWHM_{SM}$ = 2.6 mm = 25λ for NA = 0.3; and $FWHM_{PyD}$ = 2.4 mm = 23λ, $FWHM_{SM}$ = 1.4 mm = 14λ for NA = 0.5, Fig. 6(d)-(f)). The lower FWHM results in better axial signal confinement and more detailed sectioning.

Higher NAs further enhance the lateral resolution of LFI imaging systems (Fig. 7(a)). Inspection of subwavelength features of a resolution target is possible via the incorporation of a 0.5 NA, presenting noticeable improvement upon the 0.3 NA used when inspecting the system's PSF. The modulation transfer function (MTF) is computed to determine the lateral resolution (Fig. 7(b)). The lateral resolution surpasses the diffraction limit [54] for all NAs of 0.5, 0.3, 0.15, and 0.07. We achieve resolutions of 0.68λ, 0.92λ, 1.71λ, and 2.35λ, while the diffraction-limited values are λ, 1.67λ, 3.33λ, and 7.14λ, respectively (Fig. 7(c)). Such improvement to subwavelength levels is attributed to two main factors: the pinhole effect from the QCL's waveguide upon reinjection, and a nonlinearity order of 2.9 between the detection signal and the target's reflectance. The

Optics EXPRESS

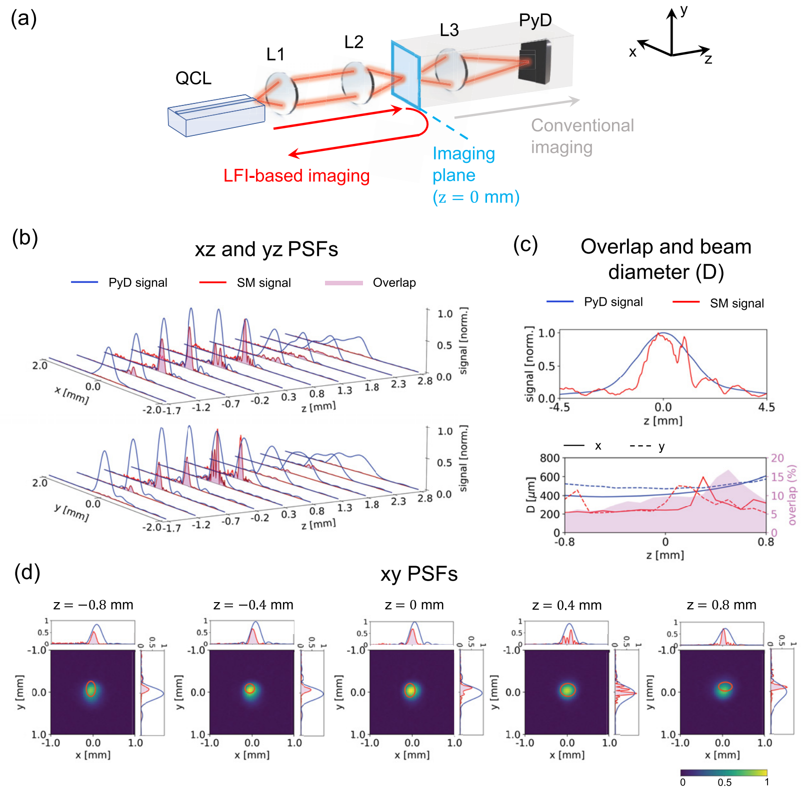

Fig. 5. Comparison between conventional and LFI imaging PSFs near the imaging plane. (a) Optical scheme illustrating LFI and conventional imaging configurations. (b) 3D PSF of conventional imaging (PyD signal, blue) and LFI imaging (SM signal, red) for planes near the imaging plane ($z = 0$ mm). (c) PSF along the optical axis (z) and lateral beam diameters (D) are computed to assess axial and lateral resolutions for both systems. (d) Reinjected beam diameters (red circles) superimposed on the xy focused beam profile (Fig. 3(b)). The overlap percentage is calculated as $100 \times [A_{\text{overlap}}/(A_{\text{PyD}} + A_{\text{SM}} - A_{\text{overlap}})]$.

observed nonlinearity arises from changes in the self-mixing waveform as target reflectivity increases. As the feedback strengthens, the waveform becomes increasingly tilted, leading to saturation of the equivalent receiver mixer and a growing contribution from higher-order harmonics. While confocal pinhole filtering results in a maximum resolution improvement of $\sqrt{2}$ or 1.4, the nonlinear effects boost the resolution further by a factor of $\sqrt{2.9}$ or 1.7 beyond the diffraction limit. This agrees well with the experimental observations illustrated in Fig. 7(c), explaining the better than twofold resolution improvement over conventional imaging.

6. 3D imaging and phase-defined depth of focus

Earlier in the paper, we demonstrated that LFI detection significantly reduces the confocal DOF compared to conventional detection schemes. However, relying solely on amplitude information overlooks one of the key advantages of our coherent imaging approach. In this study, we use a focusing NA of 0.3 (which provides a DOF equal to 25λ) to image a PCB with an area of several square centimeters and use the phase information to analyze subwavelength features within a packaged chip. This example highlights the substantial enhancement in DOF achieved through

Optics EXPRESS

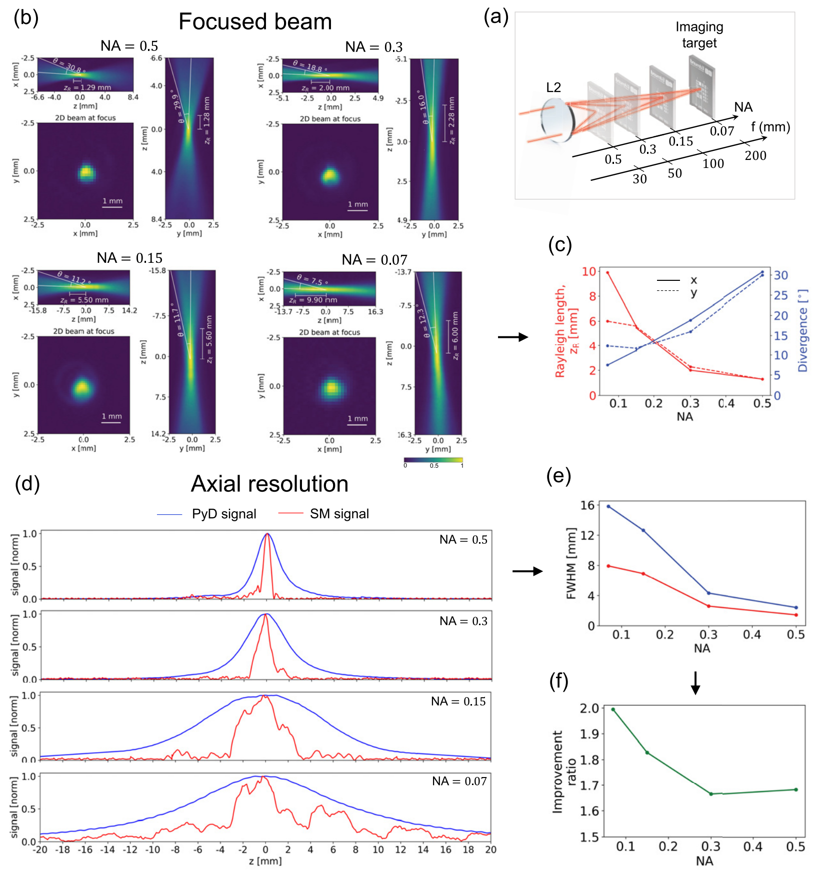

Fig. 6. Dependence of beam properties and axial resolution on the numerical aperture of the focusing lens L2. (a) Different focusing lens apertures are used to inspect the focused beam properties and axial resolution of the system. (b) Measured 3D focused beam profiles for different NAs. (c) Rayleigh length and divergence angle of the 3D focused beam profiles for each NA. (d) PyD and SM signals recorded along the optical axis (z) for different NAs. (e) The FWHM and (f) the improvement factor ($FWHM_{PyD}/FWHM_{SM}$) for each NA.

phase information analysis. By incorporating phase, we reduce the confocal DOF from 25λ to $\lambda/5$.

For 3D imaging, fast beam steering is achieved by continuous raster scanning of the target using a high-speed galvanometer mirror (OIM2002, Optics in Motion Inc., CA, USA), starting from the upper-left corner and progressing horizontally across each row before moving to the next. This enables the continuous scanning of 500 rows in 150 seconds (3.3 rows per second). A 0.5 Megapixel image is acquired in 2.5 minutes by employing a pulsed laser with a 500 ns pulse duration and a 30% duty cycle. Each pixel is averaged 16 times, yielding an effective pixel rate of 3333 pixels per second. The acquisition speed is limited by the mechanical system.

Phase and amplitude information is acquired by computing the FFT of the self-mixing waveform, with the implementation of phase interferometry algorithms to enhance axial resolution. The algorithm captures the phase shift of the SM waveform and converts it to a depth measurement by knowing that a 2π shift corresponds to the distance between two SM fringes, which translates to a half-wavelength measurement [34,55].

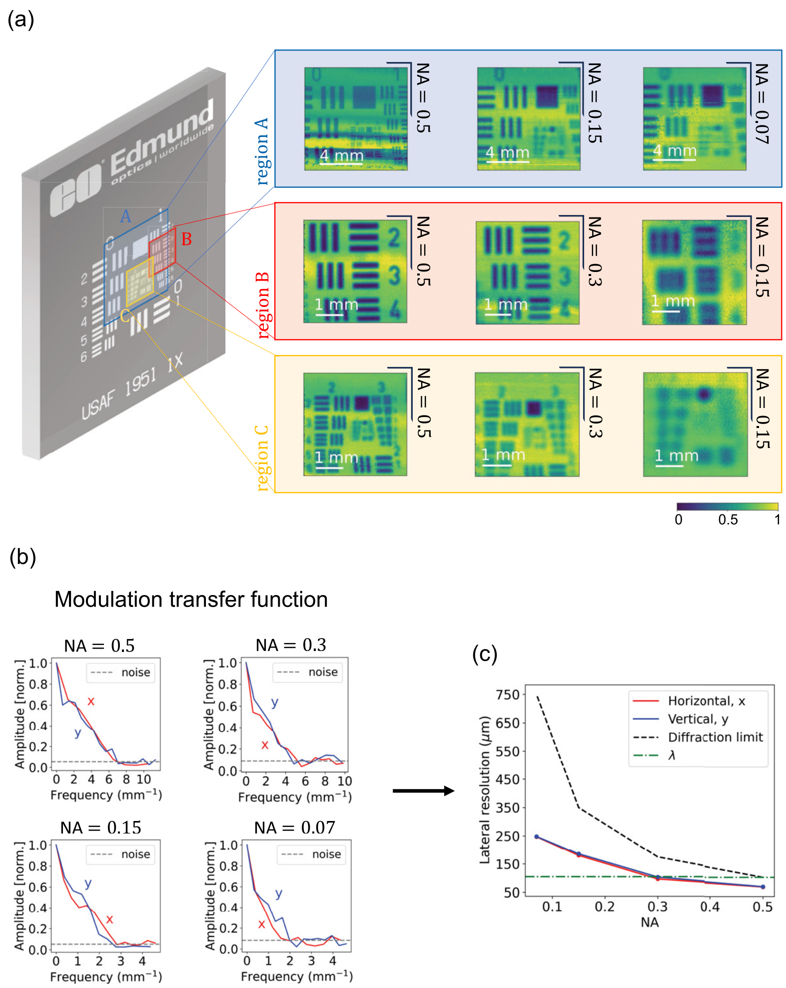

Fig. 7. Dependence of lateral resolution on the numerical aperture of the focusing lens L2. (a) LFI imaging of different areas of a resolution target (2" × 2" Negative USAF 1951 Hi-Resolution Target, Edmund Optics, NJ, USA) for different focusing NAs. (b) Computation of the modulation transfer function (MTF) for each NA. (c) Lateral resolution of the system for each NA.

Figure 8 provides a detailed view of the same PCB, focusing on two regions of interest (ROI-1 and ROI-2). The extracted depth profiles for ROI-1 and ROI-2, corresponding to the PCB tracks and the bonding pads of the chip package, reveal intricate structural details. From the line plots it can be concluded that converting phase contrast information to an equivalent height achieves a resolution of $\lambda/5$. Figure 9 demonstrates the effectiveness of combining phase and amplitude in a single image to highlight salient features. We demonstrate that it is possible to assess the internal structure of the chip using only phase information (phase image at $z = 0.8$ mm, Fig. 9(b)), enabling more accurate and detailed structural probing through improved section imaging.

7. Conclusion

In conclusion, we have demonstrated for the first time that LFI provides enhanced resolution over conventional imaging, both laterally and axially. The system's compact design, utilizing a single

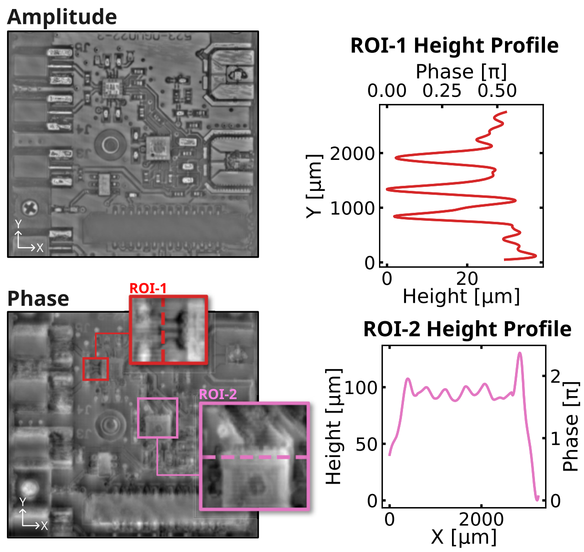

Fig. 8. Detailed view of the PCB highlighting two regions of interest (ROI-1 and ROI-2). Depth profiles for ROI-1 (PCB tracks) and ROI-2 (chip package bonding pads) demonstrate structural details and a resolution of $\lambda/5$ from phase contrast converted to equivalent height.

quantum cascade laser for illumination and detection, simplifies alignment by integrating the roles of a source, detector, and confocal pinhole within the laser itself.

Through beam propagation simulations and experimental characterization, we measured the system's PSF, revealing a better than twofold improvement in lateral and axial resolution, effectively surpassing the diffraction limit. This enhancement is attributed to two main factors: the confocal imaging configuration, where the QCL functions as an aperture—analogous to pinhole filtering in confocal microscopy—and the nonlinearity between the detected signal and the target's reflectivity, similar to multiphoton biological microscopy.

We also examined the focusing objective's numerical aperture and provided guidelines for optimizing the confocal DOF. The DOF was improved by two orders of magnitude from 25λ to $\lambda/5$ by leveraging phase information, enabling high-resolution depth sectioning. The system's capabilities were further validated through 3D tomographic imaging, uncovering previously hidden features of a packaged silicon chip with high precision using phase information.

Recent advances in THz imaging and quantum cascade lasers enable compact THz systems for real-time spectral contrast without optical delay lines, external sources, or detectors. Progress in room-temperature QCL operation and frequency combs [56–59] promises portable spectroscopic devices. The system also supports single-pixel imaging techniques, like compressed sensing [60–62] or diffractive neural networks [63], which could improve acquisition times toward real-time imaging while enabling the *modus operandi* of an actual camera.

Optics EXPRESS

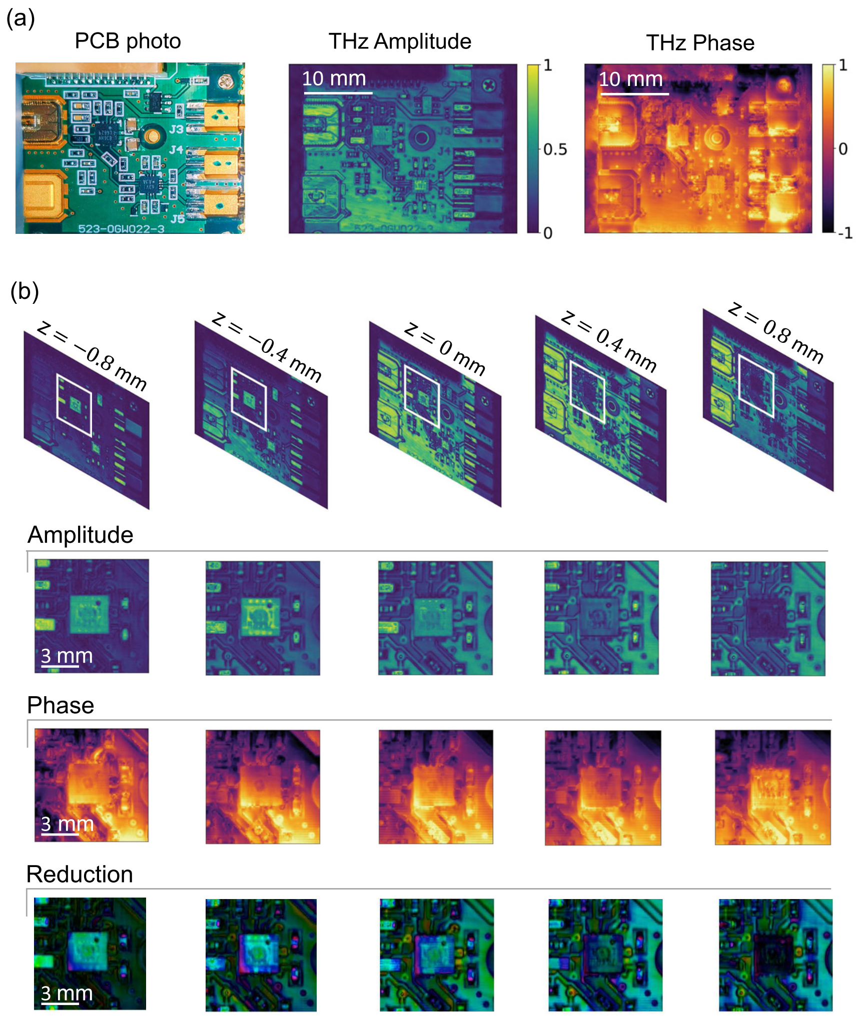

Fig. 9. LFI tomography imaging of a packaged chip. (a) LFI THz amplitude and phase images of a PCB. (b) LFI THz peak-to-peak tomography imaging of a PCB (first row), LFI THz amplitude (second row) and phase tomography imaging (third row) of one of the PCB's packaged chips (Texas Instrument LMH6629SD). The bottom row consists of reduction images, where amplitude and phase information were combined using the HSV color space (phase for hue, amplitude for value).

Funding. Australian Research Council (DE170100241, DP200101948, DP210103342, LE170100009); Engineering and Physical Sciences Research Council (EP/J002356/1, EP/P021859/1); UK Research and Innovation (MR/S016929/1); Advance Queensland (Industry Research Fellowships program).

Acknowledgments. The authors acknowledge Marcos Maestre Morote, Mickael Mounaix, Andrew Komonen, Joel Carpenter, Mayuri Kashyap and Lucas Cardoso for the helpful discussions. The authors are also thankful for the valuable contributions from the Stack Overflow community to numerous coding issues.

Disclosures. The authors declare no conflicts of interest.

Data availability. The experimental data is available in Ref. [64]. The beam propagation code is openly available in Ref. [48], and the data analysis code is available from the corresponding author upon request.

Supplemental document. See Supplement 1 for supporting content.

Optics EXPRESS

References

1. D. M. Mittleman, "Twenty years of terahertz imaging," Opt. Express **26**(8), 9417–9431 (2018).
2. H. Guerboukha, K. Nallappan, and M. Skorobogatiy, "Toward real-time terahertz imaging," Adv. Opt. Photonics **10**(4), 843–938 (2018).
3. K. B. Cooper, R. J. Dengler, N. Llombart, *et al.*, "THz imaging radar for standoff personnel screening," IEEE Trans. Terahertz Sci. Technol. **1**(1), 169–182 (2011).
4. C. L. Koch-Dandolo, T. Filtenborg, K. Fukunaga, *et al.*, "Reflection terahertz time-domain imaging for analysis of an 18th century neoclassical easel painting," Appl. Opt. **54**(16), 5123–5129 (2015).
5. A. Novikova, D. Markl, J. A. Zeitler, *et al.*, "A non-destructive method for quality control of the pellet distribution within a MUPS tablet by terahertz pulsed imaging," European J. Pharmaceutical Sci. **111**, 549–555 (2018).
6. Y. H. Tao, A. J. Fitzgerald, and V. P. Wallace, "Non-contact, non-destructive testing in various industrial sectors with terahertz technology," Sensors **20**(3), 712 (2020).
7. J.-H. Son, S. J. Oh, and H. Cheon, "Potential clinical applications of terahertz radiation," J. Appl. Phys. **125**(19), 190901 (2019).
8. A. G. Markelz and D. M. Mittleman, "Perspective on terahertz applications in bioscience and biotechnology," ACS Photonics **9**(4), 1117–1126 (2022).
9. X. Qi, K. Bertling, M. S. Stark, *et al.*, "Terahertz imaging of human skin pathologies using laser feedback interferometry with quantum cascade lasers," Biomed. Opt. Express **14**(4), 1393–1410 (2023).
10. X. Qi, K. Bertling, J. Torniainen, *et al.*, "Terahertz in vivo imaging of human skin: Toward detection of abnormal skin pathologies," APL Bioeng. **8**(1), 016117 (2024).
11. R. Ulbricht, E. Hendry, J. Shan, *et al.*, "Carrier dynamics in semiconductors studied with time-resolved terahertz spectroscopy," Rev. Mod. Phys. **83**(2), 543–586 (2011).
12. F. Mezzapesa, L. Columbo, M. Brambilla, *et al.*, "Imaging of free carriers in semiconductors via optical feedback in terahertz quantum cascade lasers," Appl. Phys. Lett. **104**(4), 041112 (2014).
13. P. Lane, P. Cunningham, J. Melinger, *et al.*, "Hot photocarrier dynamics in organic solar cells," Nat. Commun. **6**(1), 7558 (2015).
14. J. D. Buron, D. H. Petersen, P. Bøggild, *et al.*, "Graphene conductance uniformity mapping," Nano Lett. **12**(10), 5074–5081 (2012).
15. R. Al Hadi, H. Sherry, J. Grzyb, *et al.*, "A 1 k-pixel video camera for 0.7–1.1 terahertz imaging applications in 65-nm CMOS," IEEE J. Solid-State Circuits **47**(12), 2999–3012 (2012).
16. N. Oda, S. Kurashina, M. Miyoshi, *et al.*, "Microbolometer terahertz focal plane array and camera with improved sensitivity in the sub-terahertz region," J. Infrared, Millimeter, Terahertz Waves **36**(10), 947–960 (2015).
17. F. Sizov, "Terahertz radiation detectors: the state-of-the-art," Semicond. Sci. Technol. **33**(12), 123001 (2018).
18. M. Locatelli, M. Ravaro, S. Bartalini, *et al.*, "Real-time terahertz digital holography with a quantum cascade laser," Sci. Rep. **5**(1), 13566 (2015).
19. N. V. Petrov, M. S. Kulya, A. N. Tsypkin, *et al.*, "Application of terahertz pulse time-domain holography for phase imaging," IEEE Trans. Terahertz Sci. Technol. **6**(3), 464–472 (2016).
20. M. Yamagiwa, T. Ogawa, T. Minamikawa, *et al.*, "Real-time amplitude and phase imaging of optically opaque objects by combining full-field off-axis terahertz digital holography with angular spectrum reconstruction," J. Infrared, Millimeter, Terahertz Waves **39**(6), 561–572 (2018).
21. P. U. Jepsen, D. G. Cooke, and M. Koch, "Terahertz spectroscopy and imaging–modern techniques and applications," Laser Photonics Rev. **5**(1), 124–166 (2011).
22. J. Neu and C. A. Schmuttenmaer, "Tutorial: An introduction to terahertz time domain spectroscopy (THz-TDS)," J. Appl. Phys. **124**(23), 231101 (2018).
23. M. Koch, D. M. Mittleman, J. Ornik, *et al.*, "Terahertz time-domain spectroscopy," Nat. Rev. Methods Primers **3**(1), 48 (2023).
24. A. D. Rakić, T. Taimre, K. Bertling, *et al.*, "Swept-frequency feedback interferometry using terahertz frequency QCLs: a method for imaging and materials analysis," Opt. Express **21**(19), 22194–22205 (2013).
25. R. Köhler, A. Tredicucci, F. Beltram, *et al.*, "Terahertz semiconductor-heterostructure laser," Nature **417**(6885), 156–159 (2002).
26. B. S. Williams, "Terahertz quantum-cascade lasers," Nat. Photonics **1**(9), 517–525 (2007).
27. J. Faist, *Quantum Cascade Lasers* (Oxford University Press, 2013).
28. A. Rakić, T. Taimre, K. Bertling, *et al.*, "Sensing and imaging using laser feedback interferometry with quantum cascade lasers," Appl. Phys. Rev. **6**(2), 021320 (2019).
29. P. Dean, Y. L. Lim, A. Valavanis, *et al.*, "Terahertz imaging through self-mixing in a quantum cascade laser," Opt. Lett. **36**(13), 2587–2589 (2011).
30. P. Dean, A. Valavanis, J. Keeley, *et al.*, "Coherent three-dimensional terahertz imaging through self-mixing in a quantum cascade laser," Appl. Phys. Lett. **103**(18), 181112 (2013).
31. F. Mezzapesa, M. Petruzzella, M. Dabbicco, *et al.*, "Continuous-wave reflection imaging using optical feedback interferometry in terahertz and mid-infrared quantum cascade lasers," IEEE Trans. Terahertz Sci. Technol. **4**(5), 631–633 (2014).
32. M. Wienold, T. Hagelschuer, N. Rothbart, *et al.*, "Real-time terahertz imaging through self-mixing in a quantum-cascade laser," Appl. Phys. Lett. **109**(1), 011102 (2016).

33. E. A. Pogna, C. Silvestri, L. L. Columbo, *et al.*, "Terahertz near-field nanoscopy based on detectorless laser feedback interferometry under different feedback regimes," APL Photonics **6**(6), 061302 (2021).
34. J. Keeley, P. Dean, A. Valavanis, *et al.*, "Three-dimensional terahertz imaging using swept-frequency feedback interferometry with a quantum cascade laser," Opt. Lett. **40**(6), 994–997 (2015).
35. Y. A. García-Jomaso, D. L. Hernández-Roa, J. Gardu no-Mejía, *et al.*, "Sub-wavelength continuous THz imaging system based on interferometric detection," Opt. Express **29**(12), 19120–19125 (2021).
36. Y. Xie, Y. Wang, L. Li, *et al.*, "Realization of high depth resolution using two-beam self-mixing interferometry with a terahertz quantum cascade laser," Opt. Commun. **545**, 129737 (2023).
37. Z. Wang, X. Li, Q. Wang, *et al.*, "Terahertz super-resolution imaging based on a confocal waveguide and a slider-crank scanning mechanism," Opt. Express **31**(12), 19945–19957 (2023).
38. D. Mohun, N. Sulollari, M. Salih, *et al.*, "Terahertz microscopy using laser feedback interferometry based on a generalised phase-stepping algorithm," Sci. Rep. **14**(1), 3274 (2024).
39. Q. Li, Y. Zhou, Y.-F. Yang, *et al.*, "2.52 terahertz dual-axis reflection confocal scanning microscope," J. Opt. Soc. Am. A **33**(4), 637–641 (2016).
40. C. Ciano, M. Flammini, V. Giliberti, *et al.*, "Confocal imaging at 0.3 THz with depth resolution of a painted wood artwork for the identification of buried thin metal foils," IEEE Trans. Terahertz Sci. Technol. **8**(4), 390–396 (2018).
41. H. Momiyama, Y. Sasaki, I. Yoshimine, *et al.*, "Depth super-resolved imaging of infrastructure defects using a terahertz-wave interferometer," NDT & E Int. **120**, 102431 (2021).
42. U. S. De Cumis, J.-H. Xu, L. Masini, *et al.*, "Terahertz confocal microscopy with a quantum cascade laser source," Opt. Express **20**(20), 21924–21931 (2012).
43. W. R. Zipfel, R. M. Williams, and W. W. Webb, "Nonlinear magic: multiphoton microscopy in the biosciences," Nat. Biotechnol. **21**(11), 1369–1377 (2003).
44. D. Denkova, M. Ploschner, M. Das, *et al.*, "3d sub-diffraction imaging in a conventional confocal configuration by exploiting super-linear emitters," Nat. Commun. **10**(1), 3695 (2019).
45. P. Dean, J. Keeley, Y. L. Lim, *et al.*, *Mid-Infrared and Terahertz Quantum Cascade Lasers* (Cambridge University Press, 2023), Chap. 15, p. 477.
46. Y. L. Lim, K. Bertling, T. Taimre, *et al.*, "Coherent imaging using laser feedback interferometry with pulsed-mode terahertz quantum cascade lasers," Opt. Express **27**(7), 10221–10233 (2019).
47. M. Wienold, L. Schrottke, M. Giehler, *et al.*, "Low-voltage terahertz quantum-cascade lasers based on LO-phonon-assisted interminiband transitions," Electron. Lett. **45**(20), 1030–1031 (2009).
48. https://github.com/jrgsilv/beam-propagation.
49. X. Qi, K. Bertling, T. Taimre, *et al.*, "Terahertz quantum cascade laser under optical feedback: effects of laser self-pulsations on self-mixing signals," Opt. Express **29**(24), 39885–39894 (2021).
50. S. Ferré, L. Jumpertz, M. Carras, *et al.*, "Beam shaping in high-power broad-area quantum cascade lasers using optical feedback," Sci. Rep. **7**(1), 44284 (2017).
51. T. Taimre, M. Nikolić, K. Bertling, *et al.*, "Laser feedback interferometry: a tutorial on the self-mixing effect for coherent sensing," Adv. Opt. Photonics **7**(3), 570–631 (2015).
52. K. Ahi, "Mathematical modeling of THz point spread function and simulation of THz imaging systems," IEEE Trans. Terahertz Sci. Technol. **7**(6), 747–754 (2017).
53. J. Pawley, *Handbook of Biological Confocal Microscopy*, vol. 236 (Springer Science & Business Media, 2006).
54. A. Hon, , "The relation of aperture and power in the microscope (continued).," J. R. Microsc. Soc. **2**(4), 460–473 (1882).
55. M. Lazarus, F. Pantoja, M. Somekh, *et al.*, "New direction-of-motion doppler detector," Electron. Lett. **16**(25-26), 953–954 (1980).
56. D. Burghoff, T.-Y. Kao, N. Han, *et al.*, "Terahertz laser frequency combs," Nat. Photonics **8**(6), 462–467 (2014).
57. Q. Lu, F. Wang, D. Wu, *et al.*, "Room temperature terahertz semiconductor frequency comb," Nat. Commun. **10**(1), 2403 (2019).
58. A. Khalatpour, A. K. Paulsen, C. Deimert, *et al.*, "High-power portable terahertz laser systems," Nat. Photonics **15**(1), 16–20 (2021).
59. C. Silvestri, X. Qi, T. Taimre, *et al.*, "Frequency combs in quantum cascade lasers: An overview of modeling and experiments," APL Photonics **8**(2), 020902 (2023).
60. W. L. Chan, K. Charan, D. Takhar, *et al.*, "A single-pixel terahertz imaging system based on compressed sensing," Appl. Phys. Lett. **93**(12), 121105 (2008).
61. R. I. Stantchev, X. Yu, T. Blu, *et al.*, "Real-time terahertz imaging with a single-pixel detector," Nat. Commun. **11**(1), 2535 (2020).
62. M. Dabbicco, A. Lupo, and P. S. Labini, "Scanless optical feedback imaging principle by single-pixel compressed sensing," Appl. Opt. **60**(10), B88–B94 (2021).
63. J. Li, X. Li, N. T. Yardimci, *et al.*, "Rapid sensing of hidden objects and defects using a single-pixel diffractive terahertz sensor," Nat. Commun. **14**(1), 6791 (2023).
64. https://espace.library.uq.edu.au/view/UQ:bf3e83f.